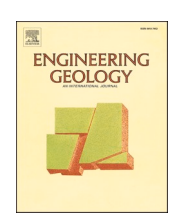
ELSEVIER

Contents lists available at ScienceDirect

## **Engineering Geology**

journal homepage: www.elsevier.com/locate/enggeo





# A unified characterization of small-strain shear modulus of sands under triaxial compression stress states

Yutang Chen a,b, Jun Yang b,\*

- <sup>a</sup> School of Civil Engineering, Suzhou University of Science and Technology, Suzhou, 215011, China
- <sup>b</sup> Department of Civil Engineering, The University of Hong Kong, Pokfulam, Hong Kong, China

#### ARTICLE INFO

Keywords: Shear modulus Anisotropic stress state Triaxial compression Initial state parameter

#### ABSTRACT

In slopes and embankments, soil elements are often anisotropically loaded and the sustained stress ratio SR may vary a lot. The understanding of the influence of SR on the small-strain shear modulus  $G_0$  of sands prior to failure is a practical concern that remains inadequately understood in the existing literature. This study aims to address this knowledge gap through a meticulously designed experimental program. The testing program encompasses three quartz sands with differing particle shapes and a diverse set of principal stress ratios produced via drained triaxial compression. By employing bender elements embedded within the apparatus, elastic shear waves are generated, enabling the measurement of  $G_0$  from isotropic stress states to anisotropic stress states. A careful evaluation and comparison of existing anisotropic  $G_0$  models in the literature is also conducted, and the potential limitations when subjected to elevated SR levels are noted. A new, unified model is proposed to effectively characterize  $G_0$  of different sands subjected to a wide range of triaxial compression states and it is validated using literature data.

## 1. Introduction

Shear wave velocity  $V_s$  and its associated small-strain shear modulus  $G_0$  of granular soil are fundamental properties in both practical applications and theoretical modeling, and the characterization of  $V_s$  and  $G_0$  through physical experiments and numerical simulations is a subject of enduring interest in soil mechanics and geotechnical engineering (Hardin and Richart, 1963; Wang and Mok, 2008; Clayton, 2011; Gu et al., 2023; Kim et al., 2023). Extensive studies documented in the literature have contributed to the recognition that  $G_0$  of sands is influenced by confining stress, packing density, sample preparation, and material characteristics (Ishibashi and Capar, 2003; Cho et al., 2006; Cabalar, 2010; Rahman et al., 2012; Fioravante et al., 2013; Yang and Gu, 2013; Wichtmann and Triantafyllidis, 2014; Altuhafi et al., 2016; Goudarzy et al., 2016; Yang and Liu, 2016; Payan et al., 2017; Shi et al., 2021; Chen and Yang, 2024a; Nie et al., 2022; Gobin et al., 2023).

The knowledge mentioned above is primarily based on the studies conducted on the isotropically confined specimens. However, in practical scenarios such as under  $K_0$  conditions or surrounding foundations, soil elements often experience anisotropic loadings due to self-weight and additional loads transferred from superstructures. This

background has spurred a series of investigations aimed at understanding the impact of stress anisotropy on  $G_0$  (Hardin and Black, 1966; Roesler, 1979; Tatsuoka et al., 1979; Yu and Richart, 1984; Ishibashi et al., 1991; Santamarina and Cascante, 1996; Ezaoui and Di Benedetto, 2009; Escribano and Nash, 2015; Payan et al., 2016; Goudarzy et al., 2018; Jafarian et al., 2018; Prashant et al., 2019; Bayat and Ghalandarzadeh, 2020; Dutta et al., 2021; Kaviani-Hamedani et al., 2021; Shi et al., 2022; Zhang et al., 2022; Shirkavand and Fakharian, 2023). For instance, Payan et al. (2016) conducted constant p' compression tests on various quartz sands and observed an increase in  $G_0$  (measured by bender elements) with increasing stress ratio SR, where SR is defined as the ratio of effective axial stress  $\sigma'_a$  and effective radial stress  $\sigma'_r$  and p'represents the mean effective stress. Similar conclusions were reached by Jafarian et al. (2018) when measuring  $G_0$  of carbonate sands using the resonant column method under similar loading conditions. Tatsuoka et al. (1979) employed cyclic torsional shear tests to compare  $G_0$  of different Toyoura specimens subjected to the same p' but varying SR. They found that  $G_0$  initially increased when SR increased to 1.5, but subsequently decreased with further increases in SR, with a reduction of approximately 20%20 % when SR reached 5. A similar trend of  $G_0$ initially increasing and then decreasing with SR was also observed by

E-mail address: junyang@hku.hk (J. Yang).

<sup>\*</sup> Corresponding author.

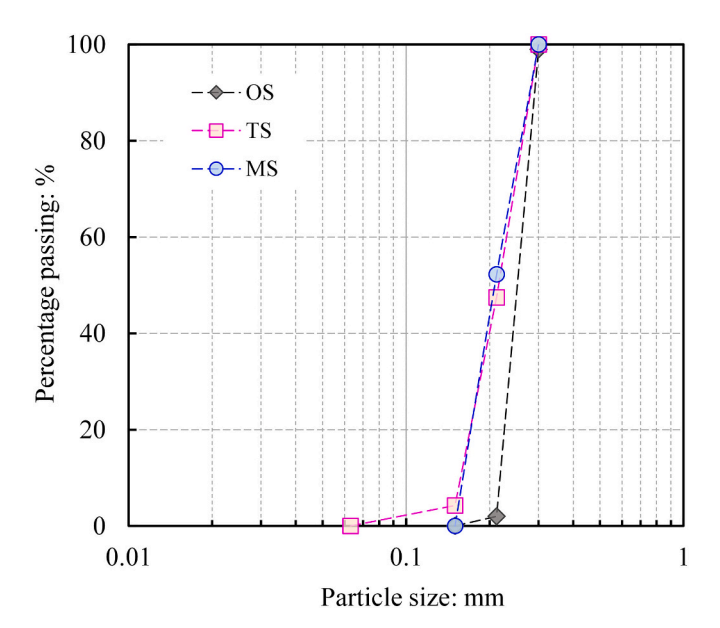


Fig. 1. Particle size distributions of testing materials.

Goudarzy et al. (2018) during  $G_0$  measurements of Hoston sand using the resonant column method under a constant p' compression stress path. Yu and Richart (1984) conducted resonant column tests on anisotropically loaded quartz sands and found that the measured  $G_0$  values could only be accurately captured by the modified Hardin model when the applied SR was within 2, otherwise, the measured values deviated significantly from the calculated values.

The existing literature on the effects of stress ratio SR on  $G_0$  displays some inconsistencies, which may be attributed to the varying ranges of SR applied in different studies. For example, Payan et al. (2016) and Jafarian et al. (2018) utilized SR values below 2.5 and 2.8, respectively. In contrast, Yu and Richart (1984) and Tatsuoka et al. (1979) examined specimens with SR levels reaching up to 5. The choice of maximum SR for a given specimen is not arbitrary, but rather constrained by the initial conditions such as packing density and confining stress level (Been and Jefferies, 1985; Yang and Li, 2004; Lashkari et al., 2017). In triaxial compression, loose sand specimens are unable to sustain a stress ratio higher than the critical state stress ratio  $SR_{cs}$ , but dense sand specimens can withstand a higher SR up to the peak stress ratio SR<sub>max</sub> (Yang and Li, 2004). The critical state friction angle  $\varphi_{cs}$  can be used to convert  $SR_{cs}$ , with the relationship  $SR_{cs} = (1 + \sin\varphi_{cs})/(1-\sin\varphi_{cs})$ . It should be noted that  $\varphi_{cs}$  is influenced by material characteristics, and for quartz sand,  $\varphi_{cs}$ typically exceeds 30°, corresponding to an SR<sub>cs</sub> of 3 (Yang and Li, 2004; Cho et al., 2006; Shin and Santamarina, 2013; Yang and Luo, 2015). Considering that the sustained SR in soil elements may vary widely from loose deposits to dense deposits, it becomes crucial to understand the evolution of  $G_0$  as SR transitions from low to high values for design and evaluation purposes. However, this aspect is not yet well addressed in the current literature.

In order to address the aforementioned concerns, a comprehensive experimental program has been conducted using a triaxial apparatus equipped with bender element functions. Key features of the experimental program include: (a) the investigation of three quartz sands with distinct particle shapes under saturated conditions, with meticulous monitoring of volume variations during loading; (b) the exploration of a diverse array of initial specimen conditions in terms of void ratio and confining pressure; and (c) the incorporation of a wide range of triaxial compression stress states utilizing a specifically designed loading scheme. The evaluation of  $G_0$  of specimens at different anisotropic stress states is achieved by the elastic shear waves generated by bender elements. The main results of the experimental program, along with a detailed interpretation and discussion are presented in this paper.

**Table 1** Physical properties of tested materials.

Sand	Angularity	$G_s$	$\varphi_{\rm cs}$ (0)	$e_{ m max}$	$e_{\min}$
OS TS MS	Rounded Sub-rounded to sub-angular Angular	2.66 2.64 2.66	29.9 31.4 35.0	0.879 0.977	0.592 0.605

Note: TS = Toyoura sand; MS = Manufactured silica sand; OS = Ottawa sand;  $G_s$  = specific gravity;  $\varphi_{cs}$  = critical state friction angle ( $^0$ );  $e_{max}$  = maximum void ratio;  $e_{min}$  = minimum void ratio.

Additionally, an in-depth examination and comparison of existing anisotropic  $G_0$  models in the literature are provided, highlighting their potential deficiencies especially when subjected to the high SR level. Furthermore, a unified model is proposed for characterizing  $G_0$  of different sands subjected to various triaxial compression states.

## 2. Testing programs

## 2.1. Materials and sample preparation

The present study employs three different types of sand, namely Ottawa sand (OS), Toyoura sand (TS), and manufactured silica sand (MS). MS is an artificial crushed silica sand with angular particles. TS and OS are natural sands that have been extensively investigated in the literature. TS is characterized by sub-rounded and sub-angular particles, whereas OS comprises predominantly rounded particles. The size distribution curves of the three sands are shown in Fig.1 and their physical properties are summarized in Table 1. Note that values of  $\varphi_{cs}$  were determined through drained triaxial compression tests on loose specimens with an axial strain value of approximately 27 %. The effect of particle shape on  $\varphi_{cs}$  (Yang and Luo, 2015) is evident, with the most angular MS sand exhibiting the highest value of  $\varphi_{cs}$ .

The dry deposition method, a commonly employed technique for sand specimen preparation, was utilized in this study. In this method, based on the desired void ratio, a predetermined mass of dry sand is slowly deposited into a split mold through a glass funnel, without any falling height. The deposited sand is then carefully leveled and compacted by tapping the side of the mold with a rubber tamper, thus achieving the desired density for the specimen. It should be noted that the conventional procedure may not be suitable for preparing highly dense specimens. To overcome this limitation, very dense specimens are prepared by employing a five-layer approach, with each layer reconstituted using the aforementioned procedure. In this study, all specimens were tested under saturated conditions. To ensure proper saturation, the specimens were flushed with carbon dioxide and de-aired water, followed by the application of back pressure. Specimens with a Skempton B-value greater than 0.95 were considered fully saturated.

## 2.2. Loading schemes and wave measurement

The experimental setup for measuring shear wave velocity involved the utilization of piezoelectric bender elements, which were embedded in both the bottom pedestal and top cap of a triaxial apparatus, as depicted in Fig. 2. The specimens used in the testing had a diameter and height of 50 mm and 100 mm, respectively. To induce anisotropic stress conditions, the effective radial stress  $\sigma_r'$  was maintained at a constant value while the effective axial stress  $\sigma_a'$  was incrementally increased. The increment in  $\sigma_a'$  was divided into two stages. In the first stage,  $\sigma_a'$  was incrementally raised to achieve the predetermined SR values of 1.3, 1.6, 1.9, 2.2, 2.5, and 2.8, and shear wave measurements were conducted at each SR. It is worth noting that the maximum SR employed in the first loading stage (2.8) was intentionally kept lower than the critical stress ratio  $SR_{CS}$  of the three types of sands, thereby ensuring that the specimens would not experience failure. In the second loading stage, further increases in SR were achieved through strain-controlled drained shear at

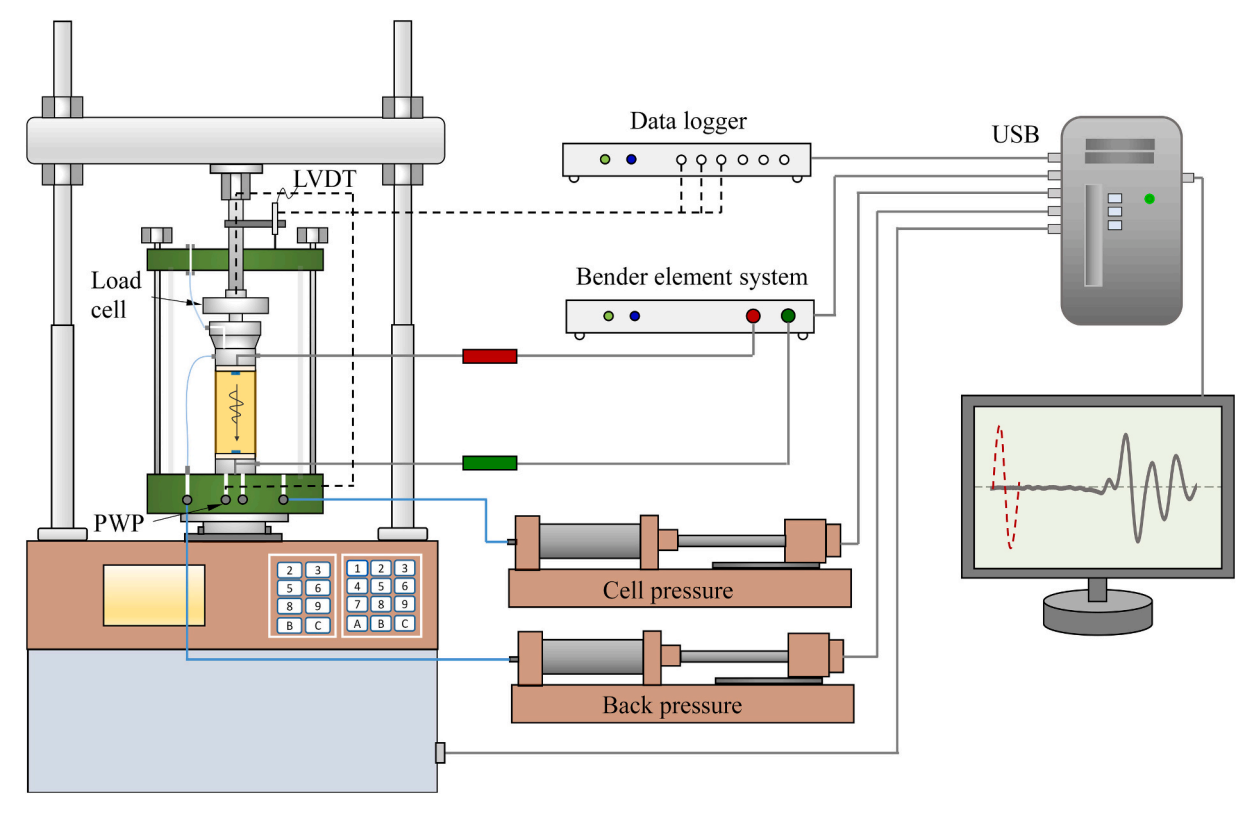


Fig. 2. Schematic drawing of triaxial apparatus with bender element testing.

**Table 2**Summary of anisotropic loading test series.

Testing sand	$\sigma_r^{\prime}$ (kPa)	$e_0$	$D_r$ (%)	$[G_0]_{ini}$ (MPa)	Applied SR range
TS	100	0.698	75	120.0	1-4.58
TS	200	0.834	38	112.0	1-3.33
TS	200	0.770	56	128.9	1-3.61
TS	200	0.696	76	160.9	1-4.16
TS	200	0.640	91	181.7	1-4.92
TS	400	0.847	35	142.1	1-3.24
TS	400	0.843	36	143.2	1-3.21
TS	400	0.833	39	142.0	1-3.23
TS	400	0.700	74	223.3	1-3.98
OS	100	0.633	86	120.0	1-4.35
OS	200	0.630	87	165.3	1-4.25
OS	400	0.747	46	156.9	1-3.22
MS	100	0.929	_	78.2	1-5.13
MS	100	0.959	_	72.9	1-4.79
MS	200	0.951	-	108.3	1-4.65
MS	200	0.903	-	110.8	1-4.83
MS	400	1.064	-	111.7	1–3.57

Note: (TS = Toyoura sand; MS = manufactured silica sand; OS = Ottawa sand;  $\sigma'_r$  = effective radial stress (kPa);  $e_0$  = post-isotropic consolidation void ratio;  $D_r$  = relative density (%);  $[G_0]_{ini}$  = initial  $G_0$  value at isotropic confining (MPa)).

a rate of 0.1 %/min, which was to ensure a stable response of both loose and dense specimens. Shear wave measurements were performed at specific time intervals during this stage. Similar testing methods have been used in the literature to measure  $V_s$  and  $G_0$  during cyclic and monotonic loadings (Lee and Huang, 2007; Park and Santamarina, 2019; Prashant et al., 2019; Ueno et al., 2019; Dutta et al., 2021; Kaviani-Hamedani et al., 2021; Li et al., 2023). Note that the two anisotropic loading stages in this study were both controlled under drained conditions such that no excess pore pressure was generated during the anisotropic loading. For dense specimens exhibiting clear strain-softening behavior, only data points obtained prior to reaching

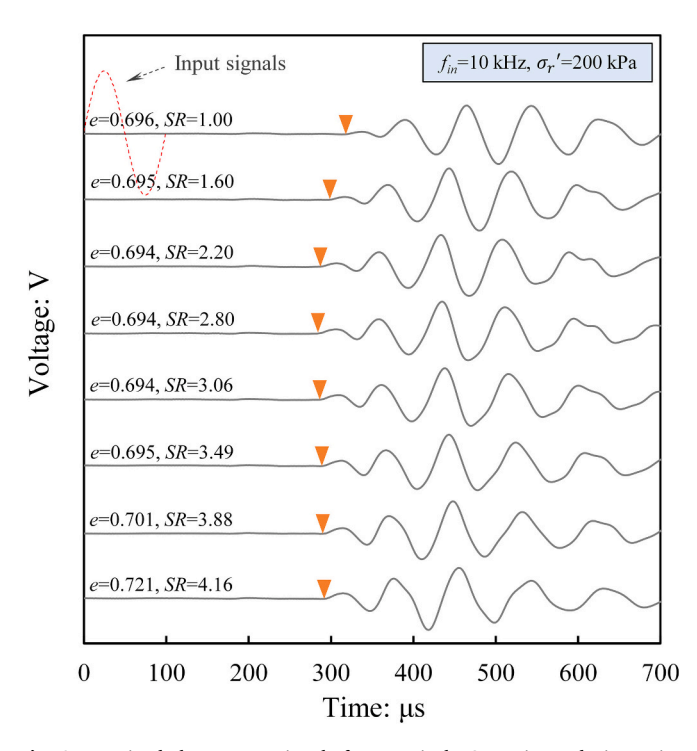


Fig. 3. Received shear wave signals for a typical TS specimen during anisotropic loading.

the peak stress ratio were used for analysis. On the other hand, for loose specimens showing strain-hardening behavior, only data points corresponding to axial strains less than 10 % were utilized. The specific testing series conducted in this study are outlined in Table 2.

Fig. 3 presents the obtained shear wave signals for a Toyoura sand

**Table 3** Fitting parameters of A and n in Eq. (2) for three sands.

Testing sand	A: MPa	n
OS	76.7	0.45
TS	87.6	0.43
MS	98.6	0.43

Note: TS = Toyoura sand; MS = Manufactured silica sand; OS = Ottawa sand.

specimen under various anisotropic stress conditions. A consistent arrival of shear waves was observed when an excitation frequency of 10 kHz was adopted. The determination of wave travel time was conducted using the first arrival in the time domain, which has shown promise in previous studies (Gu et al., 2015; Alvarado and Coop, 2012; Lee and Huang, 2007). A comprehensive investigation of different methods of data interpretation can be referred to Yamashita et al. (2009) and Yang and Gu (2013). In Fig. 3, the first arrivals in the received signals were

indicated using a downward triangle marker, allowing for the calculation of wave velocities based on the tip-to-tip distance between the source and receiver elements. During the whole testing process, the tip-to-tip distance is varied due to specimen deformation and can be updated based on the installed LVDT (linear variable differential transformer). Thus, the shear modulus is obtained based on the following equation:

$$G_0 = \rho V_s^2 \tag{1}$$

where  $\rho$  is the effective density taking into account the dispersion of shear waves in saturated permeable materials (Youn et al., 2008; Gu et al., 2015). Note that with the experimental setup in Fig. 2, the shear wave propagates in the vertical (axial) direction and polarizes in the horizontal direction, giving  $G_0 = G_{\rm vh}$ , and that the measured  $G_0$  represents constant-fabric, small-strain property of the specimen at the particular stress state.

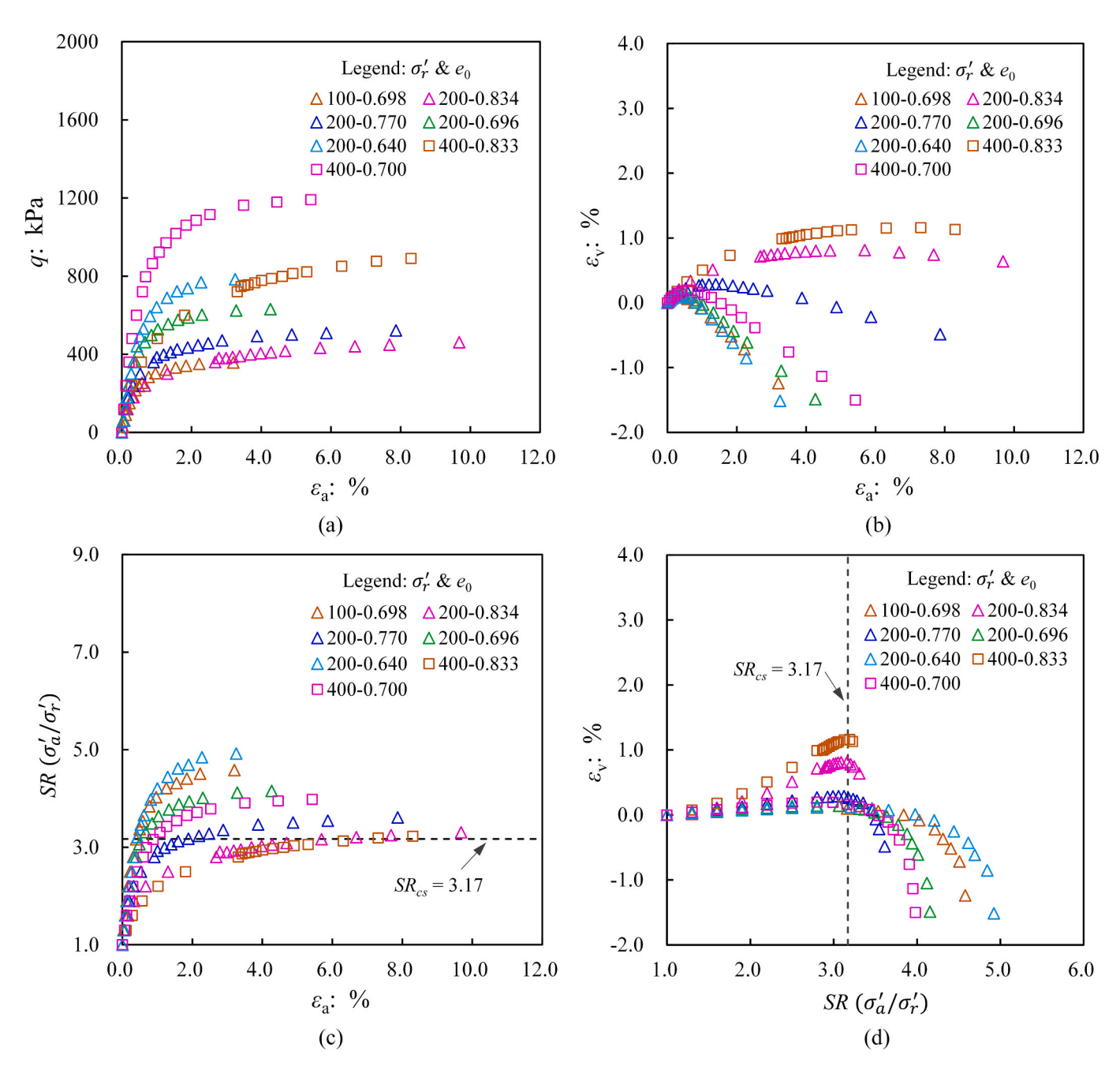


Fig. 4. Mechanical responses of TS during anisotropic loading: (a) q versus  $\varepsilon_a$ ; (b)  $\varepsilon_v$  versus  $\varepsilon_a$ ; (c) SR versus  $\varepsilon_a$  (d)  $\varepsilon_v$  versus SR.

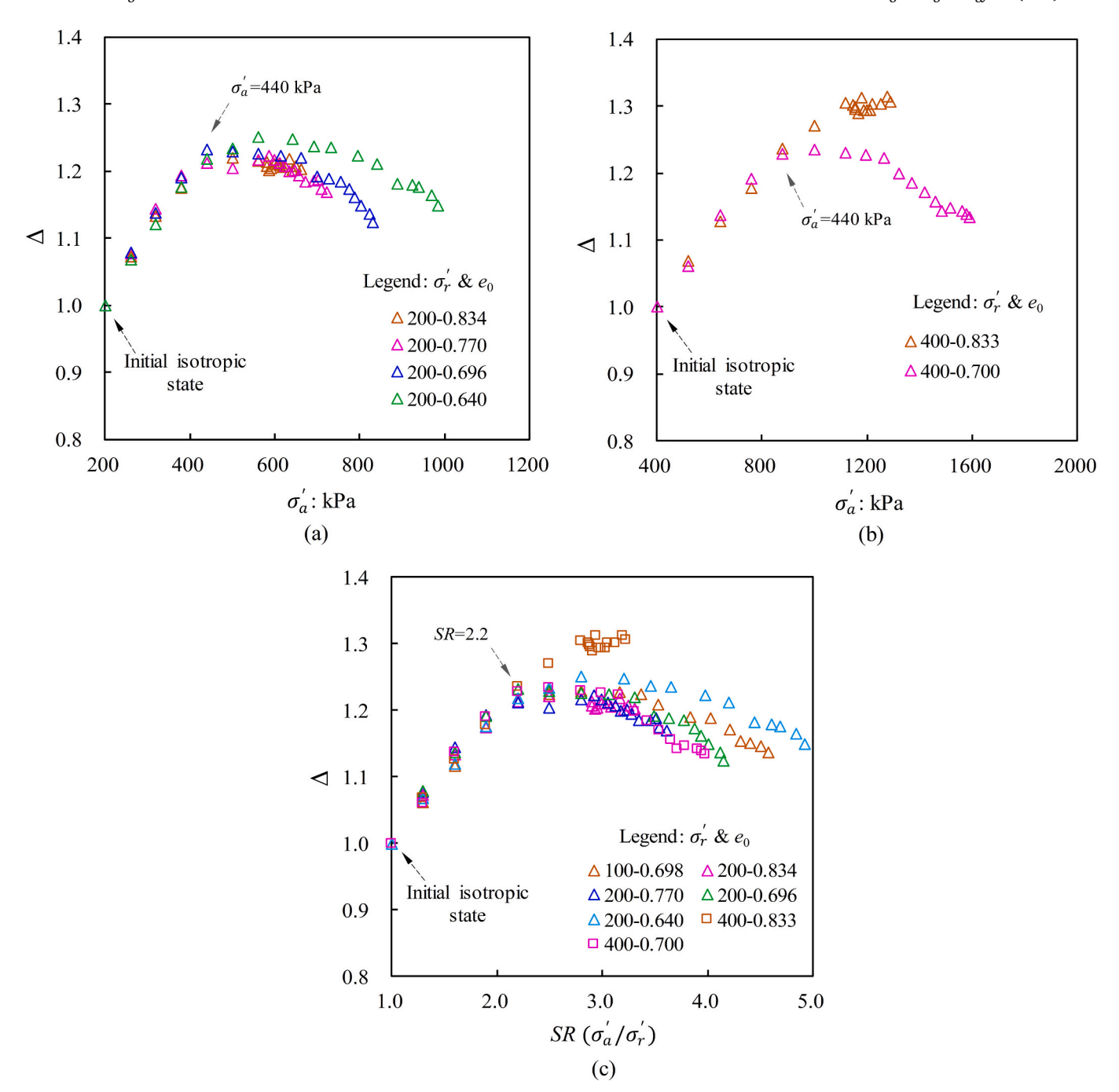


Fig. 5. Variation of Δ with effective axial stress  $\sigma'_a$  and stress ratio SR of TS: (a) Δ versus  $\sigma'_a$  at  $\sigma'_r$ =200 kPa; (b) Δ versus  $\sigma'_a$  at  $\sigma'_r$ =400 kPa; (c) Δ versus SR at both  $\sigma'_r$ =200 kPa and 400 kPa.

To better investigate  $G_0$  under anisotropic conditions, a comprehensive series of tests were first conducted under various isotropic confining stresses, namely 50 kPa, 100 kPa, 200 kPa, and 400 kPa. This allowed for the establishment of a reference dataset of  $G_0$  for the three testing sands under isotropic confining conditions. The obtained data was then fitted to the Hardin's model, represented by Eq. (2):

$$G_0 = A \cdot F(e) \cdot \left(\frac{\sigma'}{p_a}\right)^n \tag{2}$$

Where  $\sigma$ ' represents the effective isotropic confining stress;  $p_a$  is the reference stress and is taken as 98 kPa; F(e) is the void ratio function and is chosen to follow the form  $F(e)=(2.17\text{-}e)^2/(1+e)$ ; A and n are the two best-fit constants determined for each sand and their respective values

are listed in Table 3.

## 3. Tests results and analysis

## 3.1. Evolutions of $G_0$ under anisotropic loading

To facilitate discussion, Fig. 4 shows the mechanical responses of Toyoura sand specimens subjected to anisotropic loadings across various initial states. Each data point in Fig. 4 corresponds to the specific state at which  $G_0$  was measured. It is pertinent to note that all  $G_0$  data presented in this study are for states prior to failure. It can be seen that the SR causing the phase transformation for different specimens is generally beyond 3.

To mitigate the impact of void ratio changes induced by anisotropic

**Table 4** Detailed expressions of  $\Delta$  by literature models.

References	Expressions of $\Delta$ as a function of $SR^*$
Payan et al. (2016)	$\left(\frac{2+SR}{3}\right)^{C_u^{0.12}(0.59-0.23\rho)} \cdot \left(\frac{4SR-1}{2+SR}\right)^{0.017C_u^{0.4}\rho^{-1.82}} \cdot \left(\frac{F_1(e)}{F_1(e_0)}\right) / \left(\frac{F(e)}{F(e_0)}\right)$
Jafarian et al. (2018)	$\left(\frac{SR+2}{3}\right)^{n-1} \cdot SR^{0.589}$
Goudarzy et al. (2018)	$SR^{0.14} \cdot \left(\frac{F_2(e)}{F_2(e_0)}\right) / \left(\frac{F(e)}{F(e_0)}\right)$
Yu and Richart (1984)	$\left(\frac{1+SR}{2}\right)^n \cdot \left(1-0.3\left(\frac{SR-1}{SR_{max}-1}\right)^{1.5}\right)$

Note:  $C_u$  is coefficient of uniformity of sand;  $\rho$  is regularity of sand;  $F_1(e)$ ,  $F_2(e)$  are different void ratio functions and equal  $e^{-1.29}$  and  $(2.12-e)^2/(1+e)$ , respectively; n is the fitting parameter given in Eq. (2) for Toyoura sand;  $SR_{max}$  is the peak stress ratio of the sand specimen obtained from drained triaxial compression tests.

\* Various definitions of stress ratio may be employed in different models, which are transferred into SR for standardized comparative analysis.

loading, the obtained  $G_0$  values are adjusted using the void ratio function  $F(e) = (2.17 - e)^2/(1 + e)$ . It is important to note that this F(e) was initially proposed for  $G_0$  under isotropic stress conditions and may not be entirely applicable to  $G_0$  under anisotropic conditions. The primary objective of employing the same F(e) for both isotropic and anisotropic stress states in this study is to facilitate the development of a simple model for  $G_0$  in anisotropic stress states, as demonstrated in the subsequent sections. Additionally, to effectively demonstrate the influence of stress ratio SR, the  $G_0/F(e)$  values at different states are normalized by the  $G_0/F(e)$  value at the initial isotropic state for each specimen (Payan et al., 2016; Chen and Yang, 2024b). To provide a clear representation of this normalized ratio, it is denoted as  $\Delta$ :

$$\Delta = \frac{G_0/F(e)}{[G_0]_{ini}/F(e_0)} \tag{3}$$

where the subscript ini denotes the initial isotropic stress condition and  $e_0$  is the post-isotropic consolidation void ratio. Fig. 5(a) and (b) present the relationships between  $\Delta$  and the effective axial stress  $\sigma'_{\alpha}$  for Toyoura sand specimens prepared with different post-isotropic consolidation void ratios  $e_0$  and two initial confining stresses. It is evident that, when subjected to the same effective radial stress  $\sigma'_r$ , specimens with smaller  $e_0$ exhibit the ability to sustain higher  $\sigma_a'$ . In Fig. 5(a), a notable increase in  $\Delta$  is observed for all specimens during the initial stage of increasing  $\sigma'_a$ , which can be attributed to the increase of stress component in the wave propagation direction (axial direction in this study). However, as  $\sigma'_a$ continues to increase beyond  $\sim$ 500 kPa, a prominent decrease in  $\Delta$  is evident, except for the loosest specimen (e.g.,  $e_0 = 0.834$ ). Similar trends in the  $\Delta$  response to  $\sigma'_a$  are observed in another set of specimens shown in Fig. 5(b). In the case of specimen 400-0.833, and specimen of 200–0.834, marginal changes in SR, void ratio, and  $G_0$  are noted when SR exceeds 2.8; and consequently, the fluctuation in  $\Delta$  with SR becomes minimal and tends to converge to a stable value. Furthermore, the two specimens are at rather loose state compared with other specimens, without significant dilatancy (Fig. 4b). By plotting  $\Delta$  against the SR, all data points of Toyoura sand can be collectively compared and analyzed, as depicted in Fig. 5(c). The results indicate that the variation of  $\Delta$  with SR is not significantly influenced by the initial states of the specimens when the applied SR is small, approximately less than 2.2. However, at higher SR values, the trends become different, which is likely associated with different changes of soil structure under high stress anisotropy.

## 3.2. Examination and comparison of models in the literature

Various models have been proposed in the literature to describe  $G_0$ 

under anisotropic states. These models are often expressed in different forms but can be generally converted into the functions of effective radial stress  $\sigma_r'$ , stress ratio SR and void ratio e. In order to facilitate a comprehensive and meaningful comparison of these models, these models are used to predict the  $\Delta$  values of Toyoura sand as shown in Fig. 5(c), using the definition provided in Eq. (3). The specific expressions for the calculated  $\Delta$  values according to each literature model are summarized in Table 4. The prediction by Payan et al. (2016) requires the input of the coefficient of uniformity  $C_{ij}$  and particle regularity  $\rho$ , which was defined as the arithmetic average of roundness and sphericity (Cho et al., 2006). For Toyoura sand,  $C_u$  is determined to be 1.47, and  $\rho$ can be approximated as 0.5 based on the particle shape chart provided in Payan et al. (2016). On the other hand, the predictions by Yu and Richart (1984) and Jafarian et al. (2018) depend on the stress exponent n defined in Eq. (2), and the value for Toyoura sand is 0.43. It should be noted that the prediction by Yu and Richart (1984) is specifically associated with the peak stress ratio  $SR_{max}$  of each specimen, which can be determined during the process of strain-controlled drained triaxial shear conducted in this study.

The models proposed in the literature are employed to predict the behavior of Toyoura sand specimens, as illustrated in Fig. 6. The results demonstrate notable discrepancies among the predictions of different models, particularly as the applied SR increases. In Fig. 6(a), the maximum difference in predictions reaches approximately 50 % when SR is above 4. While predictions by models of Payan et al. (2016), Goudarzy et al. (2018), and Jafarian et al. (2018) generally show an increasing trend of  $\Delta$  with SR, the magnitude of this increase varies significantly among these models. However, none of these models are able to capture the decreasing trend of  $\Delta$  observed in dense specimens at higher SR values, which may be attributed to the limited range of the applied SR values in the testing program of these studies. Additionally, the model proposed by Yu and Richart (1984) generally captures the decreasing trend of  $\Delta$  with SR in dense specimens, but its prediction for looser specimens may introduce significant errors.

#### 3.3. A unified approach to characterize SR effects

The implementation of SR in this study introduces two distinct impacts on the evolution of  $G_0$ . The first is the alteration of applied stress level caused by the increase in  $\sigma'_a$ , while the second is the potential modification of micro-scale soil structures induced by stress anisotropy. In order to eliminate the influence of stress level variations, the void ratio corrected shear modulus,  $G_0/F(e)$ , is further divided by average stress component  $\left(\left(\sigma'_a+\sigma'_r\right)/2p_a\right)^n$  according to Chen and Yang (2024b), resulting in the derivation of a stress-normalized modulus, denoted as  $G_0^*$ :

$$G_0^* = \frac{G_0/F(e)}{\left( \left( \sigma_a' + \sigma_r' \right) / 2p_a \right)^n} \tag{4}$$

where n is the stress exponent obtained from the isotropic  $G_0$  model defined in Eq. (2). Fig. 7(a) displays the variations of  $G_0^*$  with SR for different Toyoura sand specimens. To better quantify the impact of SR, a factor R, is introduced for each specimen, which represents the ratio of  $G_0^*$  and  $G_0^*$  at initial isotropic states:

$$R = \frac{G_0^*}{[G_0^*]_{ini}} \tag{5}$$

The R values obtained for different Toyoura sand specimens are presented as a function of SR in Fig. 7(b). It is evident that for applied SR values below approximately 2.2, the R value remains close to 1 across all specimens. However, as the SR continues to increase, the R value starts to decline. This degradation corresponds to the phenomenon observed in Fig. 5(c) and may hint at the possible influence of SR on the microscale structure within the specimen. Also, the extent of reduction of R

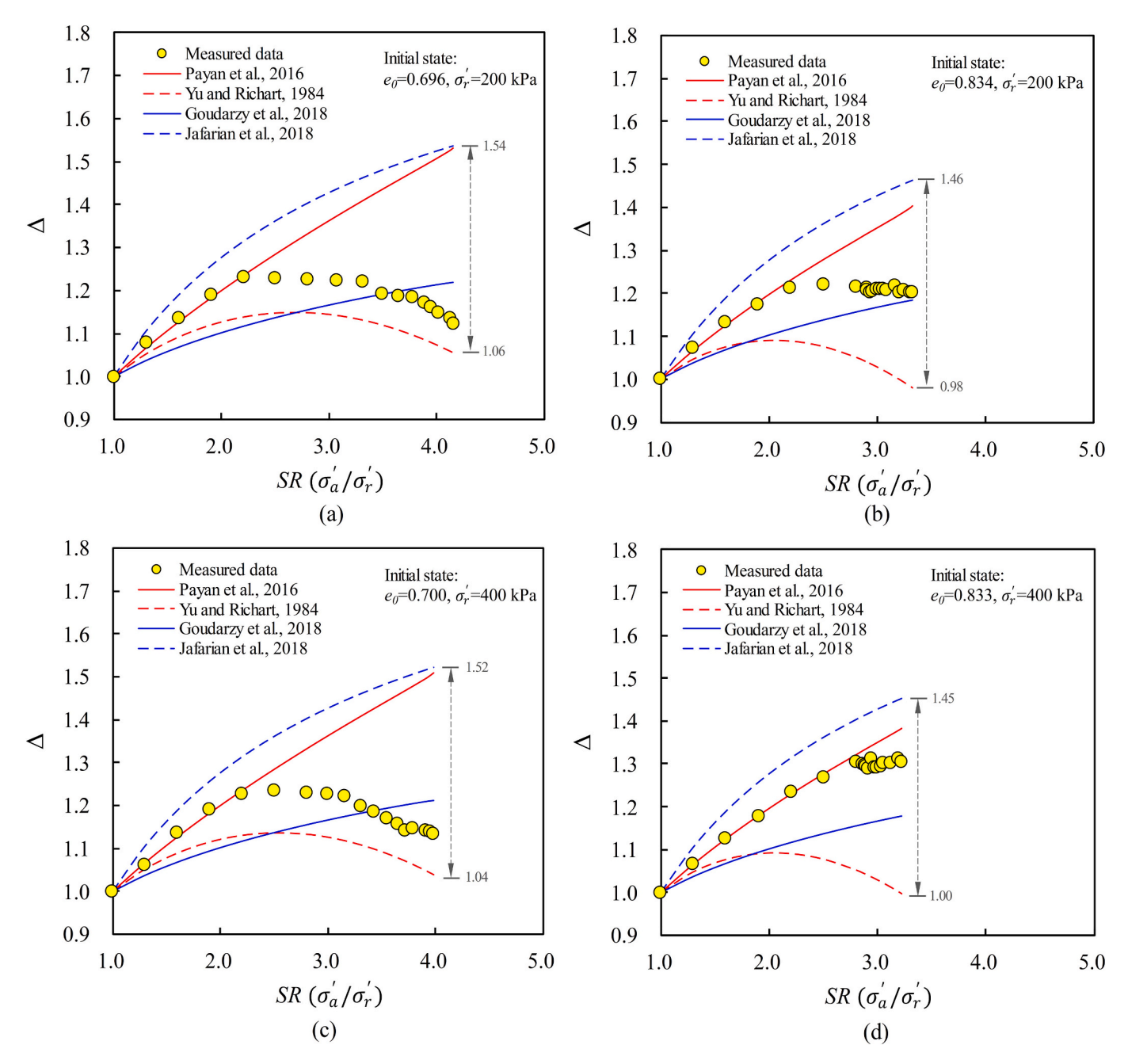


Fig. 6. Examination and comparison of the anisotropic  $G_0$  models in the literature.

appearing to be dependent on the post-isotropic consolidation void ratio  $e_0$  and initial confining stress of the tested specimen. The final recorded R value in Fig. 7(b) for each specimen is denoted as  $R_{\min}$ . Considering that R is defined as the ratio of the  $G_0^*$  under anisotropic conditions to that under isotropic conditions,  $R_{\min}$  represents the maximum degradation of  $G_0^*$  that may occur in specimens transitioning from isotropic states to all the possible pre-peak stress states. In order to provide a more comprehensive characterization of the initial state of each specimen, the initial state parameter  $\psi_0$  from critical state soil mechanics is introduced (Been and Jefferies, 1985). This parameter considers the combined influence of packing density and confining stress level, and describes the relative state of the soil specimen with respect to the critical state:

$$\psi_0 = e_0 - e_{cs} \tag{6}$$

where  $e_0$  denotes the post-isotropic consolidation void ratio and  $e_{cs}$  refers to the void ratio at the critical state line. The schematic definition of

the initial state parameter  $\psi_0$ , along with the critical state line of Toyoura sand in the e-p' space, is presented in Fig. 8, based on the results obtained from large-strain monotonic undrained shear tests conducted by Yang et al. (2022). A higher  $\psi_0$  value generally signifies a looser initial state of the specimen. The state parameter has been shown to be a useful state variable to characterize the mechanical behavior of sands under both undrained and drained conditions (Yang et al., 2022; Yang and Li, 2004).

By considering the critical state locus depicted in Fig. 8 and the initial conditions of the specimens, it becomes feasible to calculate the  $\psi_0$  value for each Toyoura sand specimen. Fig. 9 exhibits the relationship between  $R_{\rm min}$  and  $\psi_0$  for the Toyoura sand specimens. Notably, it is observed that  $R_{\rm min}$  increases with the  $\psi_0$  value, indicating that a specimen prepared at a denser initial state can have a greater degradation of  $G_0^*$ . It needs to be noted the trend line in Fig. 9 only applies to the data obtained at pre-peak stress states. The R value at post-peak stress state is

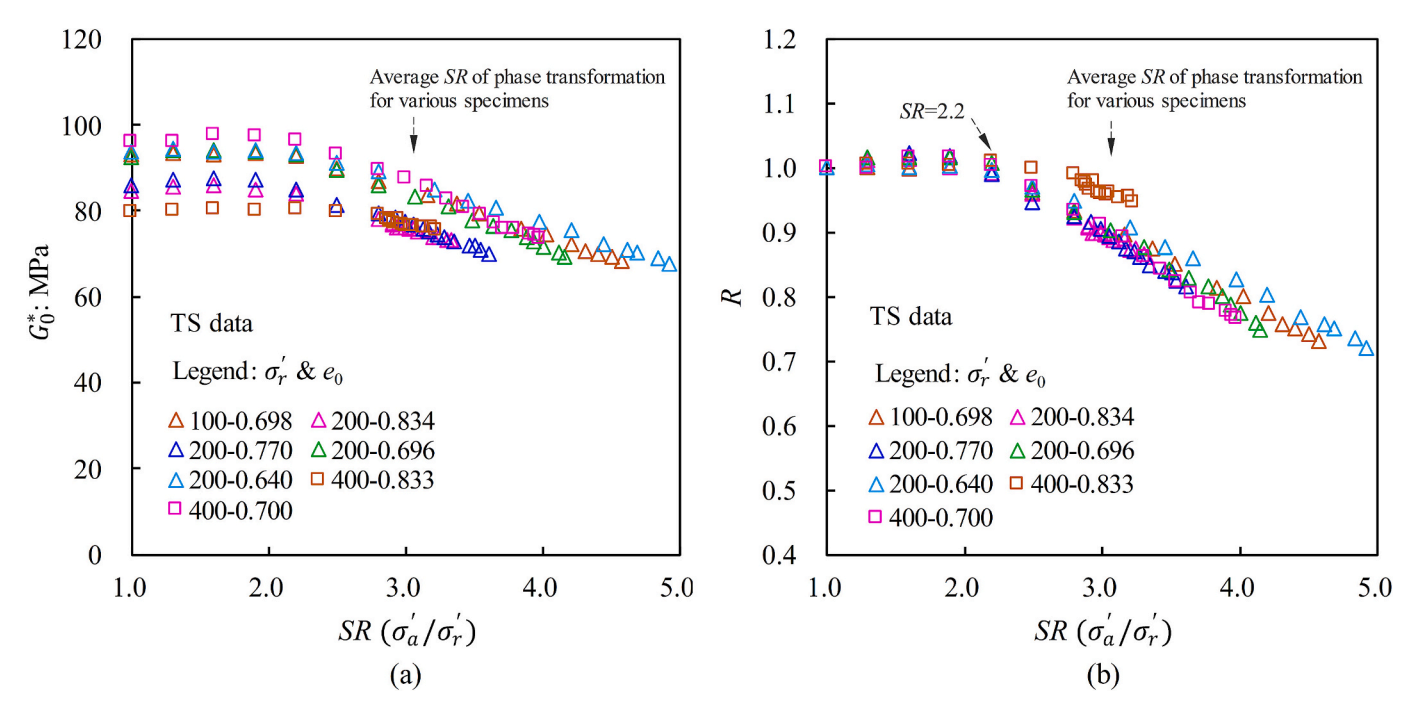


**Fig. 7.** Variations of stress normalized modulus  $G_0^*$  and the factor R with SR for TS: (a)  $G_0^*$  versus SR; (b) R versus SR.

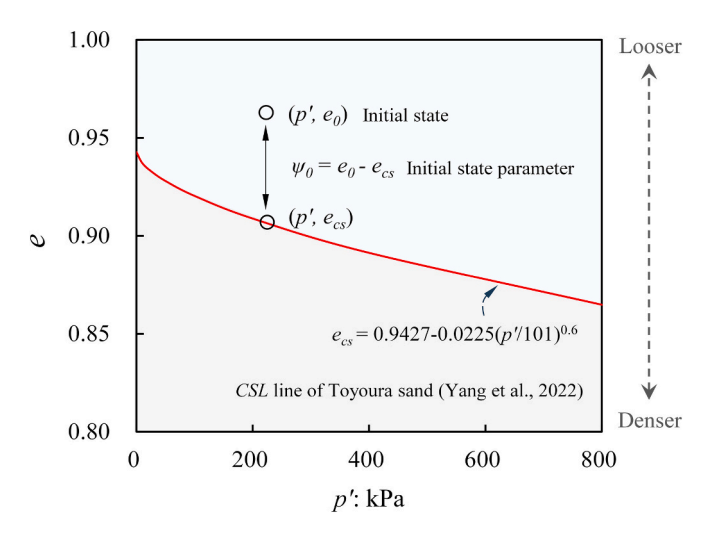


**Fig. 8.** Critical state line of TS and the definition of initial state parameter  $\psi_0$ .

not analyzed in this study, and further investigation into this aspect is worthwhile.

The typical results of R versus SR for all three sands are presented in Fig. 10. It is observed that the R value of MS sand exhibits a slower rate of reduction with increasing SR. The diminished rate of reduction can be due to the heightened shearing resistance of angular particles, which may require a higher SR threshold to induce significant modifications in the microscale structure (Gu et al., 2013; Yang and Luo, 2015). In order to account for the influence of sand type, a normalized stress ratio  $\xi$  is proposed as follows:

$$\xi = (SR - 1)/(SR_{cs} - 1) \tag{7}$$

The normalized stress ratio  $\xi$  is a crucial parameter that accounts for the influence of sand type on the variation of R values and it is noteworthy that the  $\xi$  values for different sands consistently commence at 0. When  $\xi$  is less than or equal to 1, it signifies that the applied SR is below or equal to the critical stress ratio  $SR_{cs}$ , whereas when  $\xi$  exceeds 1, it

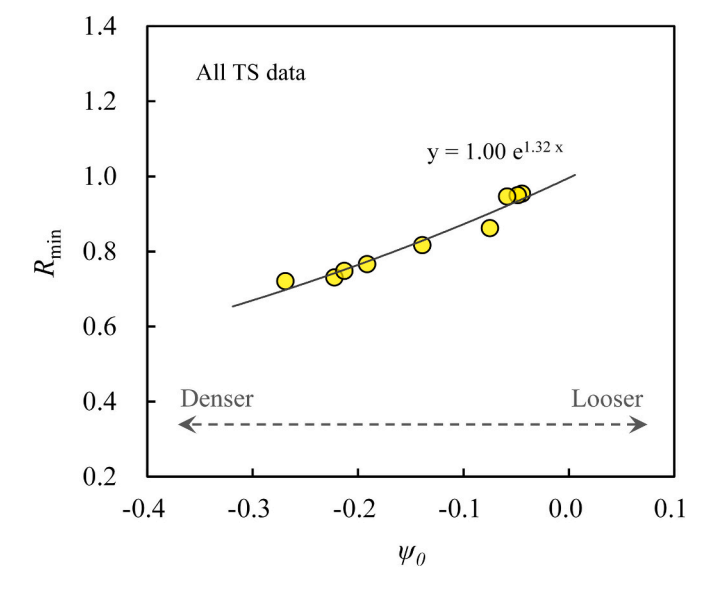


**Fig. 9.** Variation of  $R_{min}$  with initial state parameter  $\psi_0$  for TS.

indicates that the stress ratio surpasses the SRcs.

Fig. 11 presents the relationship between R values and  $\xi$  for the three sands prepared under different initial states. Remarkably, all the data points conform to a unique relationship given as follows:

$$R = 1/(1 + a\xi^b) \tag{8}$$

The best-fit parameters a and b are determined to be 0.093 and 2.864, respectively. Given that the three sands exhibit a consistent pattern, it is postulated that the values of a and b can be extrapolated to other similar sands. Furthermore, a parameter analysis is conducted here to investigate the impact of critical state friction angle  $\varphi_{cs}$  on this relationship. The results of this analysis are presented in Fig. 12.

With the definition of  $G_0^*$  and R in Eqs. (4) and (5), the following relationship can be obtained:

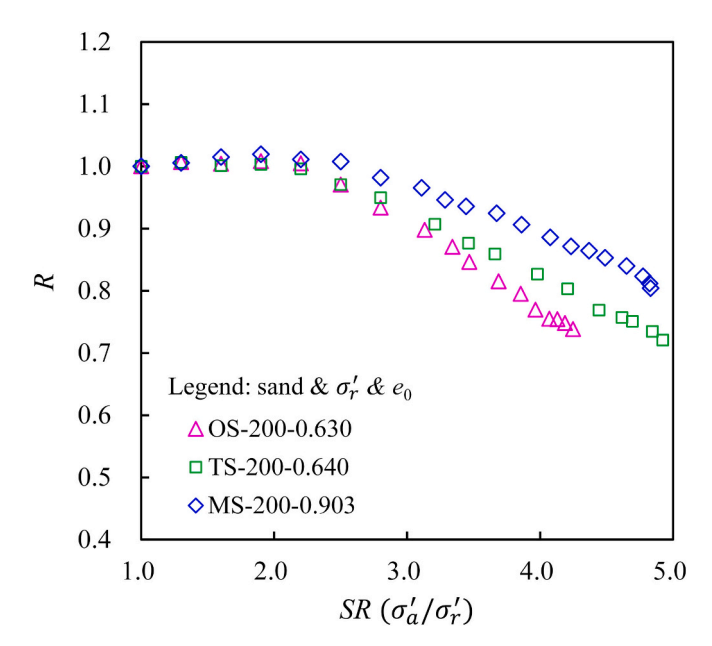


Fig. 10. Typical results of variations of R versus SR for OS, TS and MS.

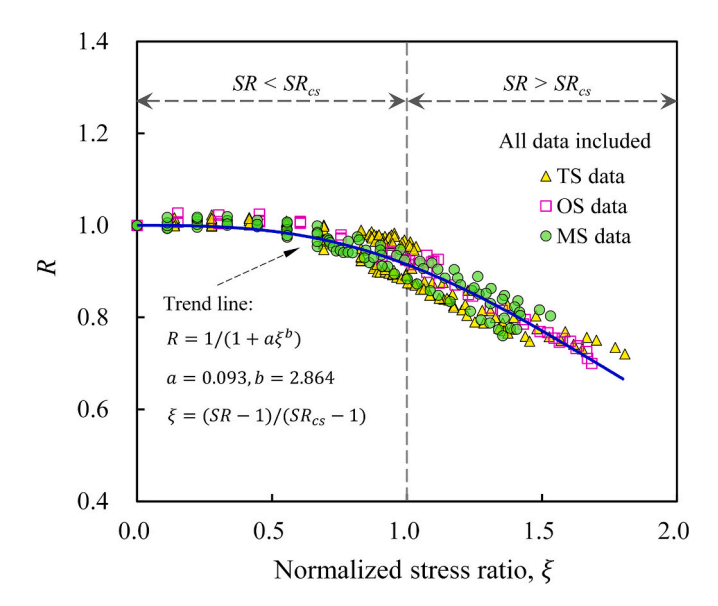


Fig. 11. Variations of R versus normalized stress ratio  $\xi$  for all the data of three testing sands.

$$G_0^* = \frac{G_0/F(e)}{((\sigma_a' + \sigma_r')/2p_a)^n} = R \cdot [G_0^*]_{ini}$$
 (9)

Based on the isotropic  $G_0$  model expressed in Eq. (2), it can be deduced that the  $\left[G_0^*\right]_{ini}$  at initial isotropic is equivalent to the value of parameter A. Consequently, a comprehensive model for  $G_0$  that encompasses both isotropic and anisotropic states can be derived:

$$G_0 = A \cdot F(e) \cdot \left( \left( \sigma_a' + \sigma_r' \right) / 2p_a \right)^n \cdot R \tag{10}$$

The predicted  $G_0$  values obtained using Eq. (10) are compared to the measured values for the three sands tested, as illustrated in Fig. 13. It is evident that there is a satisfactory level of agreement between the predicted and measured  $G_0$  values.

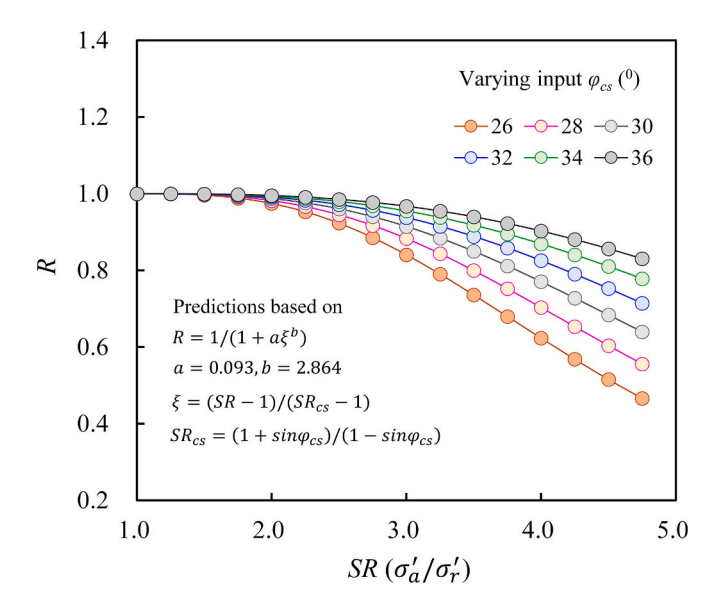


Fig. 12. A parameter analysis of the influence of  $\varphi_{\rm cs}$  on the variation of R with SR

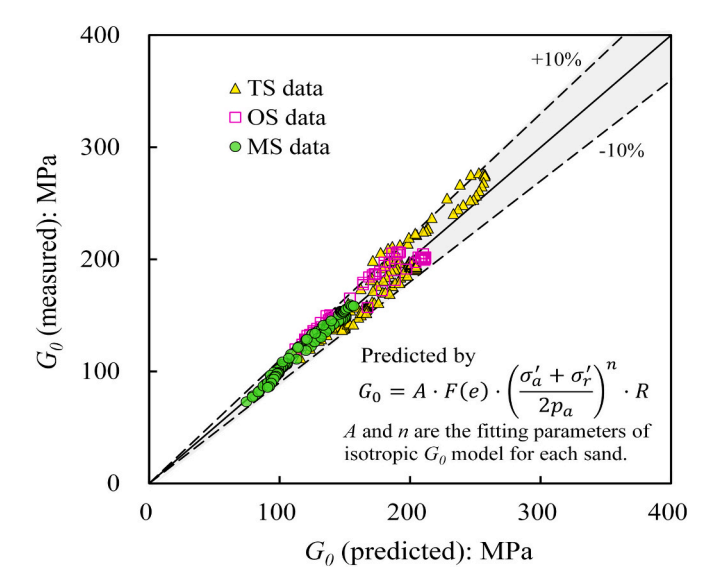


Fig. 13. Comparison of measured and predicted  $G_0$  under anisotropic states by the proposed model.

## 3.4. Validation of the proposed method

In order to examine the proposed method for characterizing the influence of stress ratio, an attempt is made to re-interpret existing literature data. Fig. 14(a) presents the re-interpreted literature data, showcasing the relationship between factor R and stress ratio SR. It should be noted that in some studies, the change in void ratio during triaxial compression loading is unavailable, thus void ratio correction is not applied. The literature data encompasses various materials such as glass beads, Hostun sand, Ottawa sand, and numerical balls from DEM (discrete element method) studies. Notably, the R values of glass beads and DEM balls in Fig. 14(a) exhibit a more rapid reduction with increasing SR compared to sands. For prediction, the value of the critical state friction angle  $\varphi_{cs}$  for each material is necessary. The  $\varphi_{cs}$  of Ottawa sand in this study is adopted for the prediction since such information is not available in the original literature. The  $\varphi_{cs}$  values for Hoston sand and glass beads are derived from the study of Escribano and Nash (2015) and Cho et al. (2006) respectively. It is assumed that the  $\varphi_{cs}$  for DEM

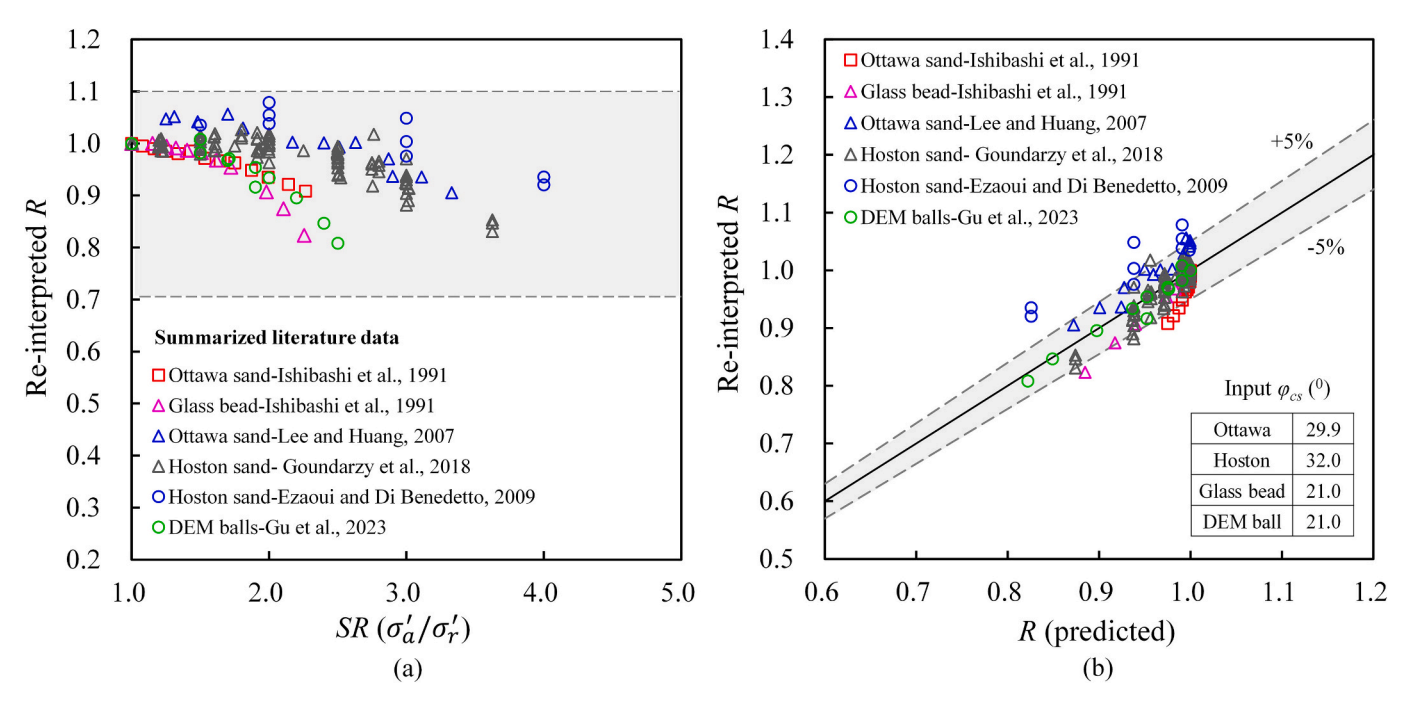


Fig. 14. Validation of the proposed approach in this study: (a) literature re-interpretation in the form of R versus SR; (b) re-interpreted R versus predicted R.

balls is the same as those for glass beads. Fig. 14(b) illustrates the comparison between the R values from the literature and the predicted R values by Eq. (8), revealing a reasonable agreement for the majority of the data. It is worth noting that the predicted R values for glass beads and DEM balls align well with the prediction, despite their distinct shapes compared to the sands tested in this study.

#### 4. Discussion

Referring to the experimental configuration depicted in Fig. 2, the  $G_0$  measured in this study is for the vertical plane (i.e.,  $G_{\rm vh}$ ). Historically, predominant focus within prior literature concerning  $G_0$  evaluation in soils has been directed towards this property, typically employing the resonant column or bender element techniques. To ascertain the shear modulus for the horizontal plane (e.g.,  $G_{\rm hh}$ ), the installation of piezoelectric transducers on the lateral boundary of the specimen is needed. While there are a few attempts in the literature (Kuwano and Jardine, 2002; Escribano and Nash, 2015), difficulties related to experimental setup and uncertainties in data acquisition and interpretation cannot be overlooked.

To transition the sample from an isotropic stress state to an anisotropic stress state, the common method is to apply the drained triaxial compression stress path, as the case of this study. Another method is to apply a nearly constant stress ratio path from the beginning, as the case of Yang and Sze (2011);  $K_0$  compression is a kind of this stress path. Several studies have indicated that the impact of stress path on the stiffness and shear behavior of sand is generally insignificant, provided that the specimen's initial state in terms of mean effective stress, deviator stress and void ratio remains similar (Yu and Richart, 1984; Payan et al., 2016).

Another interesting issue is that the stress normalized modulus  $G_0^*$  of sands demonstrates a tendency to decrease with the increase in stress ratio SR, as evidenced by data collected both in this study and from existing literature. Notably, the decrease in  $G_0^*$  with SR typically commences prior to phase transformation and peak stress ratio. This decrease in  $G_0^*$  or R indicates that, at similar void ratio and average stress level  $(\sigma_a' + \sigma_r')/2$ , the  $G_0$  under anisotropic stress conditions is smaller than that under isotropic states. This phenomenon may suggest a

potential impact of SR on the microscale structure of the specimen (Li and Dafalias, 2012; Zhao and Guo, 2013; Cheng and Wang, 2018). Several DEM simulations have suggested a close correlation between  $G_0$  and microscale coordination number CN (Gu et al., 2013; Dutta et al., 2020; Li et al., 2021; Li et al., 2023). In this regard, the reduction in  $G_0^*$  can likely be attributed to a diminution in microscale contacts resulting from the anisotropic loading. Further research is worthwhile.

## 5. Conclusion

This paper presents a comprehensive experimental investigation into the variation of small-strain shear modulus  $G_0$  of sands subjected to a wide range of anisotropic stress states prior to failure. The obtained experimental data has been thoroughly analyzed and the key findings of this study can be summarized as follows:

- (a) Under triaxial compression loading conditions where  $\sigma_{a'}$  increases and  $\sigma_{r'}$  keeps as a constant, the void ratio corrected small-strain shear modulus,  $G_0/F(e)$  exhibits an initial increase with increasing principal stress ratio, SR. This initial increase does not exhibit significant variations among specimens prepared at different post-isotropic consolidation void ratios and confining stresses. However, as the applied SR continues to increase, the increasing trend of  $G_0/F(e)$  tends to diminish. Notably, for very dense specimens,  $G_0/F(e)$  begins to decrease in the high SR range.
- (b) A comparative evaluation of existing  $G_0$  models for anisotropic stress states is presented by comparing their predictions of  $G_0/F$  (e) evolution with SR of Toyoura sand specimens. The results reveal that significant discrepancies (up to approximately 50 %) exist among the predicted values when the applied stress ratio SR is high.
- (c) The stress-normalized modulus,  $G_0^*$ , initially remains relatively constant as the stress ratio SR increases in triaxial compression loading. However, as the SR continues to increase, a reduction in  $G_0^*$  is observed. The maximum reduction of  $G_0^*$  is influenced by the post-isotropic consolidation void ratio and initial isotropic confining stress of the sand specimens. Specifically, specimens prepared at a denser initial state with a smaller initial state

- parameter,  $\psi_0$ , experience a larger reduction in  $G_0^*$  when subjected to high SR. A possible explanation of the above phenomenon is given based on the previous microscale numerical findings.
- (d) The variation of  $G_0^*$  with SR is found to be influenced by the characteristics of the testing sand, with angular sands exhibiting a slower decreasing speed of  $G_0^*$  with SR. This influence can be effectively described using the new concept, named normalized stress ratio  $\xi$ , which requires the input of critical state friction angle of each testing material. Furthermore, a unified  $G_0$  model is proposed to better characterize the  $G_0$  of different sands under anisotropic stress states, incorporating the influence of SR and material characteristics. The new model has been validated using data from various literature studies conducted on different materials including glass beads.

## CRediT authorship contribution statement

**Yutang Chen:** Writing – original draft, Investigation. **Jun Yang:** Writing – review & editing, Supervision, Funding acquisition, Conceptualization.

#### Declaration of competing interest

The authors declare that they have no known competing financial interests or personal relationships that could have appeared to influence the work reported in this paper.

## Acknowledgment

The financial support provided by the Research Grants Council of Hong Kong (C7038-20G; N-HKU723/23) is gratefully acknowledged.

### Data availability

Data that support the findings of this study are available from the corresponding author upon reasonable request.

## References

- Altuhafi, F.N., Coop, M.R., Georgiannou, V.N., 2016. Effect of particle shape on the mechanical behavior of natural sands. J. Geotech. Geoenviron. Eng. 142 (12), 04016071. https://doi.org/10.1061/(asce)gt.1943-5606.0001569.
- Alvarado, G., Coop, M.R., 2012. On the performance of bender elements in triaxial tests. Géotechnique 62 (1), 1–17. https://doi.org/10.1680/geot.7.00086.
- Bayat, M., Ghalandarzadeh, A., 2020. Modified models for predicting dynamic properties of granular soil under anisotropic consolidation. Int. J. Geomechan. 20 (3), 04019197. https://doi.org/10.1061/(asce)gm.1943-5622.0001607.
- Been, K., Jefferies, M.G., 1985. A state parameter for sands. Géotechnique 35 (2), 99–112. https://doi.org/10.1680/geot.1985.35.2.99.
- Cabalar, A.F., 2010. Applications of the oedometer, triaxial and resonant column tests to the study of micaceous sands. Eng. Geol. 112 (1–4). https://doi.org/10.1016/j.enggeo.2010.01.004.
- Chen, Y.T., Yang, J., 2024a. Small strain shear modulus of silty sands: the role of sample preparation method. Géotechnique 74 (4), 367–382. https://doi.org/10.1680/ jgeot.23.00031.
- Chen, Y.T., Yang, J., 2024b. Small-strain shear modulus of quartz sands under anisotropic stress conditions. J. Geotech. Geoenviron. Eng. 150 (5), 04024033. https://doi.org/10.1061/JGGEFK.GTENG-1216.
- Cheng, Z., Wang, J.F., 2018. Experimental investigation of inter-particle contact evolution of sheared granular materials using X-ray micro-tomography. Soils Found. 58 (6), 1492–1510. https://doi.org/10.1016/j.sandf.2018.08.008.
- Cho, G.C., Dodds, J., Santamarina, J.C., 2006. Particle shape effects on packing density, stiffness, and strength: natural and crushed sands. J. Geotech. Geoenviron. Eng. 132 (5), 591–602. https://doi.org/10.1061/(ASCE)1090-0241(2006)132:5(591).
- Clayton, C.R.I., 2011. Stiffness at small strain: research and practice. Géotechnique 61 (1), 5–37. https://doi.org/10.1680/geot.2011.61.1.5.
- Dutta, T.T., Otsubo, M., Kuwano, R., O'Sullivan, C., 2020. Evolution of shear wave velocity during triaxial compression. Soils Found. 60, 1357–1370. https://doi.org/ 10.1016/j.sandf.2020.07.008.
- Dutta, T.T., Otsubo, M., Kuwano, R., 2021. Effect of shearing history on stress wave velocities of sands observed in triaxial compression tests. Soils Found. 61 (2), 541–548. https://doi.org/10.1016/j.sandf.2021.02.002.

- Escribano, D.E., Nash, D.F.T., 2015. Changing anisotropy of G<sub>0</sub> in Hostun sand during drained monotonic and cyclic loading. Soils Found. 55 (5), 974–984. https://doi. org/10.1016/j.sandf.2015.09.004.
- Ezaoui, A., Di Benedetto, H., 2009. Experimental measurements of the global anisotropic elastic behaviour of dry hostun sand during triaxial tests, and effect of sample preparation. Géotechnique 59 (7), 621–635. https://doi.org/10.1680/geot.7.00042.
- Fioravante, V., Giretti, D., Jamiolkowski, M., 2013. Small strain stiffness of carbonate Kenya Sand. Eng. Geol. 161, 65–80. https://doi.org/10.1016/j.enggeo.2013.04.006.
- Gobin, M., Yasufuku, N., Liu, G., Watanabe, M., Ishikura, R., 2023. Small strain stiffness, microstructure and other characteristics of an allophanic volcanic ash. Eng. Geol. 313, 106967. https://doi.org/10.1016/j.enggeo.2022.106967.
- Goudarzy, M., König, D., Schanz, T., 2016. Small strain stiffness of granular materials containing fines. Soils Found. 56 (5), 756–764. https://doi.org/10.1016/j. sandf.2016.08.002.
- Goudarzy, M., König, D., Schanz, T., 2018. Interpretation of small and intermediate strain characteristics of Hostun sand for various stress states. Soils Found. 58 (6), 1526–1537. https://doi.org/10.1016/j.sandf.2018.09.002.
- Gu, X.Q., Yang, J., Huang, M.S., 2013. DEM simulations of the small strain stiffness of granular soils: effect of stress ratio. Granul. Matter 15, 287–298. https://doi.org/ 10.1007/s10035-013-0407-y.
- Gu, X.Q., Yang, J., Huang, M.S., Gao, G.Y., 2015. Bender element tests in dry and saturated sand: Signal interpretation and result comparison. Soils Found. 55 (5), 951–962. https://doi.org/10.1016/j.sandf.2015.09.002.
- Gu, X.Q., Liang, X., Hu, J., 2023. Quantifying fabric anisotropy of granular materials using wave velocity anisotropy: a numerical investigation. Géotechnique. https:// doi.org/10.1680/jgeot.22.00314.
- Hardin, B.O., Black, W.L., 1966. Sand stiffness under various triaxial stresses. J. Soil Mechan. Foundat. Divis. 92 (2), 27–42. https://doi.org/10.1061/jsfeaq.0000865
- Hardin, B.O., Richart, F.E., 1963. Elastic wave velocities in granular soils. J. Soil Mechan. Foundat. Divis. 89 (1), 33–65. https://doi.org/10.1061/JSFEAQ.0000493.
- Ishibashi, I., Capar, O.F., 2003. Anisotropy and its relation to liquefaction resistance of granular material. Soils Found. 43 (5), 149–159. https://doi.org/10.3208/ sandf.43.5 149.
- Ishibashi, I., Chen, Y.C., Chen, M.T., 1991. Anisotropic behavior of Ottawa sand in comparison with glass spheres. Soils Found. 31 (1), 145–155. https://doi.org/ 10.3208/sandf1972.31.145.
- Jafarian, Y., Javdanian, H., Haddad, A., 2018. Dynamic properties of calcareous and siliceous sands under isotropic and anisotropic stress conditions. Soils Found. 58 (1), 172–184. https://doi.org/10.1016/j.sandf.2017.11.010.
- Kaviani-Hamedani, F., Fakharian, K., Lashkari, A., 2021. Bidirectional shear wave velocity measurements to track fabric anisotropy evolution of a crushed silica sand during shearing. J. Geotech. Geoenviron. Eng. 147 (10), 04021104. https://doi.org/ 10.1061/(asce)gt.1943-5606.0002622.
- Kim, S.Y., Chun, J.K., Yeo, J.Y., Lee, J.S., 2023. Estimation of soil porosity in mine tailing using parameters from instrumented oedometer test. Eng. Geol. 317, 107065. https://doi.org/10.1016/j.enggeo.2023.107065.
- Kuwano, R., Jardine, R.J., 2002. On the applicability of cross-anisotropic elasticity to granular materials at very small strains. Géotechnique 52 (10), 727–749. https://doi. org/10.1680/geot.2002.52.10.727.
- Lashkari, A., Karimi, A., Fakharian, K., Kaviani-Hamedani, F., 2017. Prediction of undrained behavior of isotropically and anisotropically consolidated firoozkuh sand: instability and flow liquefaction. Int. J. Geomechan. 17 (10), 04017083. https://doi. org/10.1061/(ASCE)GM.1943-5622.0000958
- Lee, C.J., Huang, H.Y., 2007. Wave velocities and their relation to fabric evolution during the shearing of sands. Soil Dyn. Earthq. Eng. 27 (1), 1–13. https://doi.org/10.1016/isoildvn.2006.05.006
- Li, X.S., Dafalias, Y.F., 2012. Anisotropy at critical state: the role of fabric. J. Eng. Mech. 138 (3), 263–275. https://doi.org/10.1061/(ASCE)EM.1943-7889.0000324.
- Li, Y., Otsubo, M., Kuwano, R., 2021. DEM analysis on the stress wave response of spherical particle assemblies under triaxial compression. Comput. Geotech. 133, 104043. https://doi.org/10.1016/j.compgeo.2021.104043.
- Li, Y., Otsubo, M., Kuwano, R., 2023. Evaluation of soil fabric using elastic waves during load-unload. J. Rock Mech. Geotech. Eng. 15, 2687–2700. https://doi.org/10.1016/ j.jrmge.2022.12.004.
- Nie, J.Y., Shi, X.S., Cui, Y.F., Yang, Z.Y., 2022. Numerical evaluation of particle shape effect on small strain properties of granular soils. Eng. Geol. 303, 106652. https:// doi.org/10.1016/j.enggeo.2022.106652.
- Park, J., Santamarina, J.C., 2019. Sand response to a large number of loading cycles under zero-lateral-strain conditions: evolution of void ratio and small-strain stiffness. Geotechnique 69 (6), 501–513. https://doi.org/10.1680/jgeot.17.P.124.
- Payan, M., Khoshghalb, A., Senetakis, K., Khalili, N., 2016. Small-strain stiffness of sand subjected to stress anisotropy. Soil Dyn. Earthq. Eng. 88, 143–151. https://doi.org/ 10.1016/j.soildyn.2016.06.004.
- Payan, M., Senetakis, K., Khoshghalb, A., Khalili, N., 2017. Characterization of the small-strain dynamic behaviour of silty sands; contribution of silica non-plastic fines content. Soil Dyn. Earthq. Eng. 102, 232–240. https://doi.org/10.1016/j.soildvn.2017.08.008.
- Prashant, A., Bhattacharya, D., Gundlapalli, S., 2019. Stress-state dependency of small-strain shear modulus in silty sand and sandy silt of Ganga. Geotechnique 69 (1), 42–96. https://doi.org/10.1680/jgeot.17.P.100.
- Rahman, M.M., Cubrinovski, M., Lo, S.R., 2012. Initial shear modulus of sandy soils and equivalent granular void ratio. Geomech. Geoeng. 7 (3). https://doi.org/10.1080/ 17486025.2011.616935.
- Roesler, S.K., 1979. Anisotropic shear modulus due to stress anisotropy. In: Journal of the Geotechnical Engineering Division. 105(GT7 Proc. Paper 14692). https://doi.org/ 10.1061/ajgeb6.0000835.

- Santamarina, J.C., Cascante, G., 1996. Stress anisotropy and wave propagation: a micromechanical view. Can. Geotech. J. 33 (5), 770–782. https://doi.org/10.1139/ t96-102-323
- Shi, J.Q., Haegeman, W., Cnudde, V., 2021. Anisotropic small-strain stiffness of calcareous sand affected by sample preparation, particle characteristic and gradation. Geotechnique 71 (4), 305–319. https://doi.org/10.1680/jgeot.18.P.348.
- Shi, J.Q., Xiao, Y., Hu, J., Wu, H., Liu, H.L., Haegeman, W., 2022. Small-strain shear modulus of calcareous sand under anisotropic consolidation. Can. Geotech. J. 59 (6), 1–11. https://doi.org/10.1139/cgj-2021-0329.
- Shin, H., Santamarina, J.C., 2013. Role of particle angularity on the mechanical behavior of granular mixtures. J. Geotech. Geoenviron. Eng. 139 (2), 353–355. https://doi. org/10.1061/(ASCE)GT.1943-5606.0000768.
- Shirkavand, D., Fakharian, K., 2023. A comparison of shear modulus of unsaturated sand in triaxial and simple shear tests under different strains and suctions. Eng. Geol. 315 (20), 106972. https://doi.org/10.1016/j.enggeo.2022.106972.
- Tatsuoka, F., Iwasaki, T., Fukushima, S., Sudo, H., 1979. Stress conditions and stress histories affecting shear modulus and damping of sand under cyclic loading. Soils Found. 19 (2), 29–43. https://doi.org/10.3208/sandf1972.19.2\_29.
- Ueno, K., Kuroda, S., Hori, T., Tatsuoka, F., 2019. Elastic shear modulus variations during undrained cyclic loading and subsequent reconsolidation of saturated sandy soil. Soil Dyn. Earthq. Eng. 116, 476–489. https://doi.org/10.1016/j. soildyn.2018.10.041.
- Wang, Y.H., Mok, C.M., 2008. Mechanisms of small-strain shear-modulus anisotropy in soils. J. Geotech. Geoenviron. Eng. 134 (10). https://doi.org/10.1061/(asce)1090-0241(2008)134:10(1516).
- Wichtmann, T., Triantafyllidis, T., 2014. Stiffness and damping of clean quartz sand with various grain-size distribution curves. J. Geotech. Geoenviron. Eng. 140 (3), 6013003. https://doi.org/10.1061/(ASCE)GT.1943-5606.0000977.
- Yamashita, S., Kawaguchi, T., Nakata, Y., Mikamt, T., Fujiwara, T., Shibuya, S., 2009. Interpretation of international parallel test on the measurement of *G*<sub>max</sub> using bender elements. Soils Found. 49 (4), 631–650. https://doi.org/10.3208/sandf.49.631.

- Yang, J., Gu, X.Q., 2013. Shear stiffness of granular material at small strains: does it depend on grain size. Géotechnique 63 (2), 165–179. https://doi.org/10.1680/ geot 11 P.083
- Yang, J., Li, X.S., 2004. State-dependent strength of sands from the perspective of unified modeling. J. Geotech. Geoenviron. Eng. 130 (2), 186–198. https://doi.org/10.1061/ (asce)1090-0241(2004)130:2(186).
- Yang, J., Liu, X., 2016. Shear wave velocity and stiffness of sand: the role of non-plastic fines. Géotechnique 66 (6), 500–514. https://doi.org/10.1680/jgeot.15.P.205.
- Yang, J., Luo, X.D., 2015. Exploring the relationship between critical state and particle shape for granular materials. J. Mech. Phys. Solids 84, 196–213. https://doi.org/ 10.1016/j.jmps.2015.08.001.
- Yang, J., Sze, H.Y., 2011. Cyclic behaviour and resistance of saturated sand under nonsymmetrical loading conditions. Géotechnique 61 (1), 59–73.
- Yang, J., Liang, L.B., Chen, Y., 2022. Instability and liquefaction flow slide of granular soils: the role of initial shear stress. Acta Geotech. 17 (1), 65–79 doi:10.Y1007/ s11440-021-01200-1.
- Youn, J.U., Choo, Y.W., Kim, D.S., 2008. Measurement of small-strain shear modulus  $G_{max}$  of dry and saturated sands by bender element, resonant column, and torsional shear tests. Can. Geotech. J. 45 (10), 1426–1438. https://doi.org/10.1139/T08-069.
- Yu, P.J., Richart, F.E., 1984. Stress ratio effects on shear modulus of dry sands.
  J. Geotech. Eng. 110 (3), 331–345. https://doi.org/10.1061/(ASCE)0733-9410 (1984)110:3(331).
- Zhang, X., Liu, X., Kong, L., Wang, G., Chen, C., 2022. Small strain stiffness for granite residual soil: effect of stress ratio. Can. Geotech. J. 59 (8), 1519–1522. https://doi. org/10.1139/cgj-2021-0308.
- Zhao, J.D., Guo, N., 2013. Unique critical state characteristics in granular media considering fabric anisotropy. Géotechnique 63 (8), 695–704. https://doi.org/ 10.1680/geot.12.P.040.